

Infrared Supernova Remnants and their Infrared to X-ray Flux Ratios

Bon-Chul Koo¹, Jae-Joon Lee², Il-Gyo Jeong^{1,2}, Ji Yeon Seok³, Hyun-Jeong Kim¹

ABSTRACT

Recent high-resolution infrared space missions have revealed supernova remnants (SNRs) of diverse morphology in infrared (IR) dust emission that is often very different from their X-ray appearance. The observed range of infrared-to-X-ray (IRX) flux ratios of SNRs are also wide. For a sample of 20 Galactic SNRs, we obtain their IR and X-ray properties and investigate the physical causes for such large differences. We find that the observed IRX flux ratios ($R_{\text{IRX,obs}}$) are related to the IRX morphology, with SNRs with the largest $R_{\text{IRX,obs}}$ showing anticorrelated IRX morphology. By analyzing the relation of $R_{\text{IRX,obs}}$ to X-ray and IR parameters, we show that the $R_{\text{IRX,obs}}$ of some SNRs agree with theoretical ratios of SNR shocks in which dust grains are heated and destroyed by collisions with plasma particles. For the majority of SNRs, however, $R_{\text{IRX,obs}}$ values are either significantly smaller or significantly larger than the theoretical ratios. The latter SNRs have relatively low dust temperatures. We discuss how the natural and/or environmental properties of SNRs could have affected the IRX flux ratios and the IRX morphology of these SNRs. We conclude that the SNRs with largest $R_{\text{IRX,obs}}$ are probably located in dense environment and that their IR emission is from dust heated by shock radiation rather than by collisions. Our result suggests that the IRX flux ratio, together with dust temperature, can be used to infer the nature of unresolved SNRs in external galaxies.

Subject headings: infrared: ISM – ISM: supernova remnants – shock waves

1. Introduction

Supernova remnants (SNRs) are one of prominent objects in IR emission. ¹ In the Milky Way, among the three hundred known SNRs, about 20%–30% are usually seen in unbiased surveys using the the *Infrared Astronomical Satellite (IRAS)*, *Spitzer Space Telescope*, and *AKARI* (Arendt 1989; Saken et al. 1992; Pinheiro Gonçalves et al. 2011; Jeong et al. 2012). This low fraction,

¹Department of Physics and Astronomy, Seoul National University, Seoul 151-742, Korea; koo@astro.snu.ac.kr

²Korea Astronomy and Space Science Institute 776, Daedeokdae-ro, Yuseong-gu, Daejeon 305-348, Korea

³Department of Physics and Astronomy, University of Missouri, Columbia, MO 65211, USA

¹By “infrared (IR)” in this paper, we would generally mean “far-infrared” of wavelength $\gtrsim 25 \mu\text{m}$.

however, is likely mainly because the SNRs are located in the Galactic plane where the confusion from foreground and background emission is severe. In nearby external galaxies such as the Large Magellanic Cloud (LMC), the fraction is much higher, e.g., $\sim 60\%$ (Seok et al. 2013).

A primary mechanism for the IR emission in SNRs is thermal dust emission. Dust grains swept-up by SN blast waves are heated by collisions with hot X-ray emitting plasma and emit mid- and far-infrared emission. It has been pointed out that the resulting IR dust emission is the dominant cooling mechanism for SNRs and could be more luminous than the X-ray emission in SNRs over most of its lifetime even with dust destruction taken into account (Ostriker & Silk 1973; Dwek 1981; Draine 1981). Dwek et al. (1987) and Graham et al. (1987) examined the ratio of IR-to-X-ray (IRX) fluxes of nine Galactic and four Magellanic SNRs using *IRAS* data, respectively, and they found that all the examined SNRs have ratios greater than unity, so dust IR cooling is indeed more efficient than X-ray cooling in SNRs. However, there was a large scatter in the observed ratios over three orders of magnitudes, with a majority of SNRs having ratios significantly less than the theoretical flux ratio expected for hot gas in thermal equilibrium with the dust-to-gas ratio (DGR) of the general interstellar medium (ISM). Dwek et al. (1987) pointed out that the SNRs might have low IRX flux ratios because of the destruction of dust grains by SNR shocks or the low DGR in the ambient medium, while they could have high IRX flux ratios because of the extra contribution from IR line emission and emission from dust heated by shock radiation. For large SNRs such as the Cygnus Loop, it was shown that the IR emission can be decomposed into two components: one associated with X-rays, which might be from collisionally heated dust grains, and the other associated with optical filaments, which could be heated by both collision and radiation within the filament (Arendt et al. 1992). However, with the *IRAS* data, which have a resolution of several arcminutes, it was difficult to confirm the true nature of the IR emission for most SNRs.

Practical use of the IRX flux ratio for studying dust heating and processing has been regained with sensitive, high-resolution far-infrared (FIR) data from recent high-resolution IR space missions. Dwek et al. (2008) found that in SN 1987A, the IRX flux ratio decreased significantly over three years and showed that the change is consistent with the destruction and heating of swept-up circumstellar dust behind the SN shock wave. Arendt et al. (2010) and Williams et al. (2011) derived IRX flux ratios for the SNRs Puppis A and RCW 86, respectively, which were found to be considerably smaller than the theoretical IRX flux ratio even with dust destruction taken into account, and they concluded that the DGR in the ambient medium of these SNRs should be lower than that of the general ISM by a factor of several. It is interesting that, in other studies of Galactic and Magellanic SNRs, in which the DGR is obtained by directly comparing the dust mass derived from the IR SED (spectral energy density) modeling and the X-ray emitting mass derived from X-ray spectral analysis (Blair et al. 2007; Lee et al. 2009; Borkowski et al. 2006; Williams et al. 2006, 2011), a similar conclusion was reached. Pinheiro Gonçalves et al. (2011) performed a systematic study of the SNRs in the inner Galaxy ($10^\circ \leq \ell \leq 65^\circ$ and $285^\circ \leq \ell \leq 350^\circ$, $|b| < 1^\circ$) using the *Spitzer* MIPS GAL survey (survey of the inner Galactic plane using MIPS; Carey et al. (2009)) in which they derived IRX flux ratios of 13 SNRs among the 39 SNRs that they detected.

The derived IRX flux ratio ranged from 1.6 to 240, which confirmed the earlier conclusion that the dust IR cooling is dominant over the X-ray cooling but the result was not discussed further. More recently, Seok et al. (2015) explored the IR and X-ray characteristics of the LMC SNRs, and showed that the IRX flux ratios of the LMC SNRs are systematically lower than those of the Galactic SNRs to be consistent with the low DGR in the LMC.

In this paper, we use the IR and X-ray images from recent space missions, mainly from the *Spitzer* and the *Chandra* X-ray telescope, to explore the nature of the IR emissions from SNRs and the characteristics of their IRX flux ratios. These arcsecond-resolution images make it possible to pursue the detailed investigation of the association between the IR and X-ray emissions. We limit our study to Galactic SNRs in this paper. The twenty Galactic SNRs studied in this paper are composed of eleven² SNRs studied by Pinheiro Gonçalves et al. (2011) and nine other SNRs that are well-defined in FIR band (e.g., from 20 μm to $\gtrsim 70 \mu\text{m}$). In § 2, we summarize IR and X-ray parameters of these SNRs, introducing an index for the IRX morphological correlation. It is found that the IRX flux ratio has a systematic dependence on the IRX morphology. In § 3, we compare the observed IRX flux ratios to the theoretical ratios expected for hot shocked plasma where dust grains are heated by collisions, and we show that time-dependent dust destruction and non-equilibrium ionization can explain the observed ratios of some SNRs but not for most SNRs. This result is discussed in § 4 together with their IRX morphological correlation. We will see that we can infer the natural and/or environmental characteristics of SNRs from their IRX flux ratios without a prior knowledge on them, which will be very useful to study SNRs in external galaxies where we do not have the luxury of observing their morphology.

2. Infrared and X-ray Characteristics of Supernova Remnants

2.1. Parameters of Infrared Emission

The parameters characterizing global properties of the IR emission from SNRs are the IR flux (F_{IR}) and color temperature of dust emission (T_d , hereafter ‘dust temperature’). We have derived these parameters for 13 SNRs in this work, including 11 SNRs studied by Pinheiro Gonçalves et al. (2011) and two large SNRs IC 443 and Puppis A. For the rest, we adopted the parameters obtained in previous studies.

Eleven SNRs from Pinheiro Gonçalves et al. (2011) are all covered by the MIPS GAL survey (Carey et al. 2009) and the *Herschel* infrared Galactic Plane Survey (Hi-GAL; Molinari et al. 2010). The former survey is a legacy program of the *Spitzer Space Telescope* covering the inner Galactic plane ($\ell = 0^\circ\text{--}63^\circ$ and $298^\circ\text{--}360^\circ$) in two wavebands (24 and 70 μm) using MIPS, while the latter survey is an Open Time Key Project of the *Herschel Space Observatory* covering a similar Galactic

²Among the SNRs studied by Pinheiro Gonçalves et al. (2011) (see their Table 6), G33.6+0.1 (Kes 79) and G337.2–0.7 are not included because these remnants are not clearly visible in the FIR band.

longitude range, i.e., $\ell = 0^\circ\text{--}60^\circ$ and $300^\circ\text{--}360^\circ$, in five wavebands between 70 and 500 μm using the Photodetector Array Camera and Spectrometer (PACS) and the Spectral and Photometric Imaging Receiver (SPIRE). The latitude coverage is $|b| < 1^\circ$ except for $|\ell| < 5^\circ$ where the coverage in the MIPS GAL survey is $|b| < 3^\circ$. We used the fully calibrated *Spitzer* MIPS 24 μm images (Version 3.0) and *Herschel* PACS 70 μm images (level 2.5), which are available from the *Spitzer* Heritage Archive³ and from the *Herschel* Science Archive⁴, respectively. The MIPS 24 μm and PACS 70 μm images have comparable spatial resolutions, i.e., 6'' and 5.''2. Pinheiro Gonçalves et al. (2011) derived total IR fluxes of their sources using *Spitzer* 24 and 70 μm fluxes, but we have not used *Spitzer* 70 μm images because they have considerably lower angular resolution (16'') than the *Herschel* 70 μm images and are often contaminated by artifacts. The measured 24 and 70 μm fluxes of the SNRs are listed in Table 1. For most SNRs, we simply measured the background-subtracted total flux density inside a circular area surrounding the entire SNR with the background level estimated from an annulus just outside the circle. For some SNRs, however, the contamination from the foreground and/or background emission is dominant, particularly at 70 μm , and an accurate total flux density could not be obtained from such simple analysis. If, for example, we can measure the total 24 μm flux density but can measure the 70 μm flux density of only a limited region, we scaled the measured 70 μm flux density using the (70 μm)/(24 μm) flux ratios of that area to obtain total 70 μm flux. For SNRs that required a special remedy, we have added notes in Table 1.

Two large SNRs, IC 443 and Puppis A, have been observed by Noriega-Crespo et al. (2009) and Arendt et al. (2010), respectively, using the *Spitzer* MIPS in fast scan mode. We have downloaded the archive images from the *Spitzer* Heritage Archive and derived their 24 and 70 μm fluxes as above.

Total IR fluxes and dust temperatures are derived by assuming a single-temperature dust component with a power-law opacity of index 2, i.e.,

$$\frac{F_{24}}{F_{70}} = \left(\frac{\lambda_{24}}{\lambda_{70}}\right)^\beta \frac{B_{24}(T_d)}{B_{70}(T_d)}, \quad (1)$$

and

$$F_{\text{IR}} = F_{70} \frac{\int \kappa_\nu B_\nu(T_d) d\nu}{\kappa_\nu B_\nu(T_d)} \quad (2)$$

where κ_ν ($\propto \lambda^\beta$, with $\beta = -2$) is the mass absorption coefficient, λ_{24} and λ_{70} are reference wavelengths of the 24 and 70 μm fluxes, and $B_{24}(T_d)$ and $B_{70}(T_d)$ are the Planck functions at the temperature of T_d at wavelengths λ_{24} and λ_{70} , respectively. The reference wavelengths for the *Spitzer* 24 and 70 μm fluxes are 23.68 and 71.42 μm , respectively, while it is 70.0 μm for the *Herschel* 70 μm flux. Note that F_{24} and F_{70} in the above equations are the *color-corrected* fluxes, which differ from the observed fluxes usually by no more than a few percent. The derived T_d and

³<http://sha.ipac.caltech.edu/applications/Spitzer/SHA/>

⁴<http://www.cosmos.esa.int/web/herschel/science-archive/>

F_{IR} values are listed in Table 1. For the SNRs whose parameters are adopted from previous studies, the references are given in the last column of the table. The fluxes in Table 1 should be close to the total IR fluxes of SNRs except for RCW 86, for which the value is the flux of a small portion of the SNR (see note in Table 1).

There is one caveat. At 24 and 70 μm bands, there are ionic lines which can make a significant contribution to the observed fluxes, e.g., [Fe II] 24.5 μm , [Fe II]/[O IV] 26.0 μm , [S I] 25.2 μm , and [O I] 63 μm lines. This can happen for SNRs where the shock is radiative. For Kes 17, for example, the estimated line contributions are $38 \pm 10\%$ and $16 \pm 8\%$ to the MIPS 24 and *AKARI* 65 μm fluxes, respectively (Lee et al. 2011). If we derive the IR parameters of this remnant using the continuum fluxes only, F_{IR} will be $\sim 20\%$ lower, and T_d will be 1.5 K lower than those in Table 1. Andersen et al. (2011) obtained *Spitzer* MIPS spectra of 14 Galactic SNRs with radiative shocks in dense environment, and Kes 17 has the highest line contribution to the total IR flux. Therefore, we consider that F_{IR} and T_d in Table 1 could be overestimated for some SNRs because of FIR ionic lines but the difference is probably not significant to affect our analysis in this paper.

2.2. Parameters of X-ray Emission

Essential X-ray parameters that we need in this study are the temperature of the X-ray emitting plasma (T_e) and soft-X-ray (0.3–2.1 keV) flux (F_X). Another useful parameter is the ionization timescale $\tau_{\text{ion}} \equiv \int n_e dt$ ($= n_e t$ for a constant electron density n_e), which is the ‘time’ for the plasma to have reached the current ionization state. Both the dust and gas cooling rates, and therefore the ratio of IRX fluxes, are time-dependent, and τ_{ion} can be used as a time parameter (see the next section).

X-ray parameters of the 20 SNRs are given in Table 2. For SNRs whose parameters had been derived from detailed modeling in previous studies, we adopted those parameters. The flux values in the literature are sometimes given in a different energy range than the range of 0.3 – 2.1 keV adopted in this work. For such cases, we converted the flux value in the literature to the flux of 0.3 – 2.1 keV by applying a correction factor based on the model and the model fit parameters in the literature. There are remnants where no suitable flux value was available. For these remnants, we extracted spectra of an entire remnant and conducted a spectral fitting adopting the hydrogen column density of the X-ray absorbing gas ($N(\text{H})$) from the literature. We note that the unabsorbed flux is insensitive to detailed fit parameters except for the $N(\text{H})$ value. For three remnants (G11.2–0.3, Kes 73 and RCW 103), we derived improved fit parameters by conducting a full spectral analysis. For each remnant, the spectra from smaller regions are extracted and are fit with a single non-equilibrium ionization (NEI) model. $N(\text{H})$, T_e and τ_{ion} in Table 2 represent ensembles of these values. To derive the flux, the spectrum of the entire region is extracted and fitted with $N(\text{H})$ fixed at the value from the previous step.

2.3. Infrared and X-ray Morphology of SNRs

Figure 1 shows the IR and X-ray images of the SNRs listed in Tables 1 and 2. We see that some SNRs such as Kepler, G11.2–0.3, and Puppis A have similar IR and X-ray morphology, whereas some SNRs such as 3C391, W49B, and IC 443 have either uncorrelated or anticorrelated IR and X-ray morphologies. To represent their formal resemblance in two wavebands, we use Pearson’s linear correlation coefficient between the IR and X-ray intensities as an index. The Pearson’s r is defined as the covariance of the variables divided by the product of their standard deviations, and it varies from +1 (perfect correlation) to -1 (perfect anticorrelation). It can be obtained straightforwardly once we define the pixels for correlation, e.g., using the IDL procedure CORRELATE. We use the bright pixels contributing 50% of total IR or total X-ray fluxes. That is, we first examine the cumulative brightness distribution of pixels in IR image of a source and determine the brightness level at which the cumulative flux becomes 50% of the total IR flux of the source ($I_{IR,50\%}$). The same can be done for the X-ray image to obtain $I_{X\text{-ray},50\%}$. Then the pixels for the correlation will be the ones with *either* its IR brightness greater than $I_{IR,50\%}$ *or* its X-ray brightness greater than $I_{X\text{-ray},50\%}$. The adopted percentage (i.e., 50%) is somewhat arbitrary, but it yields correlation coefficients that reasonably characterize the morphological relation between the bright IR and X-ray emissions dominating the fluxes. Before deriving the correlation coefficient, we remove strong point sources in the IR and X-ray images and subtract a constant background. We also convolved the IR and X-ray images to the same resolution of $6''\text{--}10''$ for sources from *Chandra/XMM* images and $30''$ for sources from *ROSAT* X-ray images and resampled them onto the same grid to have the same pixel scale of $1''\text{--}5''$ per pixel depending on the image size. The computed correlation coefficients r_{50} are listed in Table 3, while Figure 2 shows the scattered diagrams of IR versus X-ray brightnesses used for the computation of r_{50} for Puppis A and W49B which have the largest positive (0.76) and the largest negative (-0.59) r_{50} , respectively.

The SNRs with relatively large ($\gtrsim 0.3$) positive r_{50} are Kepler, G11.2–0.3, G15.9+0.2, Kes 73, Kes 75, the Cygnus Loop, Cas A, Puppis A, MSH 11–54, RCW 86 and RCW 103. All these SNRs appear to have similar IR and X-ray morphologies in Figure 1. The SNRs with relatively large ($\lesssim -0.3$) negative r_{50} are 3C391, W49B, W44, and Kes 17. All these SNRs appear to have anticorrelated IR and X-ray morphology in Figure 1. The SNRs 3C396, 3C397, Tycho, IC 443, and G349.7 have r_{50} close to 0 (i.e., -0.16 to 0.20). These SNRs seem to have both correlated and anticorrelated components (see Fig. 1). We emphasize that the correlation coefficients in Table 3 are based on the images in Figure 1 which are mostly *Spitzer* $24\ \mu\text{m}$ and *Chandra* $0.3\text{--}2.1\ \text{keV}$ images (see the caption of Figure 1). If there are more than one heating mechanism for dust, they could depend on wavelength.

We note that the SNRs with large negative r_{50} belong to the category of “thermal composite” or “mixed-morphology” SNRs (hereafter MM SNRs) that appear shell or composite type in radio but with thermal X-rays inside the SNR (Rho 1995; Rho & Petre 1998), e.g., 3C391, W44, and IC 443. The IR morphologies of these SNRs are very similar to their radio morphologies, which explains their large negative r_{50} . The correlation coefficient r_{50} of the MM SNRs, which gives, in a

sense, the degree of mixed morphology, ranges from -0.59 to -0.15 excluding G292.0+1.8 which has an unusually large positive $r_{50}(= 0.46)$. Most of these SNRs are thought to be middle-aged SNRs interacting with dense ISM, e.g., molecular clouds, and the origin of center-filling thermal X-rays is considered to be either dense clumps evaporating inside hot plasma or the result of large-scale conduction (White & Long 1991; Cox et al. 1999; Vink 2012). However, not all SNRs interacting with MCs are MM SNRs and vice versa, so their nature is still unclear. For example, G292.0+1.8 is a young SNR of mixed morphology because of thermal X-rays from SN ejecta and the swept-up circumstellar medium. (It also has a large positive r_{50} .) We will discuss the nature of the SNRs with large negative r_{50} further in § 4.

3. IRX Flux Ratio and Collisional Dust Heating

In this section, we first obtain the IRX flux ratios of SNRs and investigate the relation to their IRX morphology. We then compare the observed IRX flux ratios to the theoretical ratios expected for hot shocked plasma where dust grains are heated by collisions. We note that the theoretical IRX flux ratios of hot dusty plasma are not applicable for some SNRs, e.g., young SNRs such as Tycho where the X-ray emission is mostly from shocked SN ejecta while the FIR emission is from shocked ambient medium or evolved SNRs such as IC 443 where the FIR emission is mostly from radiatively heated dust. We will see that the IRX flux ratios of such SNRs are significantly different from theoretical IRX flux ratios, so that, even without a prior knowledge, one can infer the natural or/and environmental characteristics of an SNR from its IRX flux ratio.

3.1. IRX Flux Ratio $R_{\text{IRX,obs}}$

We define the observed IRX flux ratio as

$$R_{\text{IRX,obs}} \equiv \frac{F_{\text{IR}}}{F_{\text{X}}}, \quad (3)$$

and the $R_{\text{IRX,obs}}$ of 20 SNRs obtained from F_{IR} and F_{X} in Tables 1 and 2 are given in Table 3. $R_{\text{IRX,obs}}$ ranges from 0.32 to 204. For comparison, Dwek (1987) and Pinheiro Gonçalves et al. (2011) obtained < 2.5 to 990 and 1.6–240, respectively. For some SNRs, our values differ from those of previous results by more than an order of magnitude, e.g., ours : those of Pinheiro Gonçalves et al. (2011) are 0.32:6.2 (3C397), 15.5:1.6 (RCW 103), and 62.6:5.1 (W49B). The difference from Pinheiro Gonçalves et al. (2011) values originates mostly from the adopted X-ray fluxes. Pinheiro Gonçalves et al. (2011) used the X-ray fluxes in the *Chandra* SNR catalog⁵, some of which need to be updated. The difference from the values of Dwek (1987), however, is partly due to different definitions of IRX flux ratios. Dwek (1987) used X-ray fluxes corrected for NEI effects and, for

⁵ <http://hea-www.cfa.harvard.edu/ChandraSNR/>

young SNRs such as Tycho and Cas A, they used X-ray fluxes from the swept-up ambient medium while we simply used total fluxes. These factors, which need to be considered in interpreting the IRX flux ratios, are discussed in the following sections.

Figure 3 plots $R_{\text{IRX,obs}}$ versus r_{50} . We note that the $R_{\text{IRX,obs}}$ values of the SNRs with negative r_{50} are generally larger than those of the SNRs with positive r_{50} , or, alternatively, the SNRs with high ($\gtrsim 30$) $R_{\text{IRX,obs}}$ values have $r_{50} \leq 0$. This suggests that the large scatter could at least be partly explained by the IR emission from these SNRs being of different origin, e.g., the SNRs of large negative r_{50} and high $R_{\text{IRX,obs}}$ values are MM SNRs (marked by squares in the figure) where the IR emission is probably from radiatively-heated dust *not* from collisionally-heated dust in X-ray emitting plasma (see § 4.2). Previous studies showed that the $R_{\text{IRX,obs}}$ values of SNRs are > 1 , from which they concluded that dust IR cooling dominates over the X-ray cooling (e.g., Dwek 1987; Pinheiro Gonçalves et al. 2011). All except two in our sample have $R_{\text{IRX,obs}} > 1$ which is consistent with the conclusion of previous studies. We have two SNRs, i.e., 3C397 (0.32) and Tycho (0.74), that have $R_{\text{IRX,obs}} < 1$, but they might have additional X-ray emission (see § 4.1).

3.2. Collisional Heating of Dust Grains

In Figure 4-(a), we plot $R_{\text{IRX,obs}}$ versus the temperature of hot gas T_e for 20 SNRs. The figure is similar to Figure 1 of Dwek (1987), but there are now 20 SNRs (compared to their 9) and their locations in the diagram have been largely shifted. We first note that there is a large scatter in the observed IRX flux ratio: SNRs of the same X-ray temperature ($\sim 10^7$ K) have $R_{\text{IRX,obs}}$ values that differ by more than two orders of magnitude. The dotted line in Figure 4-(a) represents the expected IRX ratios for hot, dusty plasma *in thermal and collisional equilibrium* (see Dwek 1987). If the plasma is in thermal equilibrium, its cooling rate by dust emission is equal to the heating rate of dust by collisions with electrons, so that the dust cooling function Λ_d ($\text{erg cm}^3 \text{ s}^{-1}$) becomes independent of n_e and n_H but depends on gas temperature T_e and dust composition and size. If the plasma is in collisional equilibrium (CIE), the X-ray (0.3–2.1 keV) gas cooling function Λ_X is also a function of T_e only. We have calculated the theoretical IRX ratio $R_{\text{IRX,coll}} \equiv \Lambda_d/\Lambda_X$, and the dotted line is for the ISM dust model of Weingartner & Draine (2001), who assumed that 70% of C atoms are locked in graphite grains and all Si atoms are locked in silicate (MgFeSiO_4) grains. For the grain size distribution, we adopted the MRN size distribution (Mathis et al. 1977), with minimum and maximum grain radii of $0.001 \mu\text{m}$ and $0.5 \mu\text{m}$, respectively. For Λ_X , we have used the CHIANTI code (V7.1.4; Landi et al. 2012) assuming the solar abundance of Asplund et al. (2009). We note that, by assuming solar abundance for the hot gas, we repeatedly include heavy elements in gas and dust cooling rates. However, if $R_{\text{IRX,coll}}$ is to be compared to the ratio of IR and X-ray fluxes obtained from the entire SNR, this is not an entirely unacceptable assumption. Furthermore, the physical condition for the shocked gas is expected to be very different from this equilibrium condition anyway (see below). Figure 4-(a) shows that all SNRs except W44 are below the dotted line.

The equilibrium curve in Figure 4-(a), however, is not applicable to the IRX flux ratio of SNRs for at least two reasons: First, dust grains are destroyed behind the shock front and therefore the DGR decreases with time. Second, it takes time for the swept-up ions to reach CIE, so the X-ray cooling rate at the beginning could be much lower or higher than that in the CIE model. We have developed a simple plane-shock model to calculate time-dependent $R_{\text{IRX, coll}}$ curve. (Similar models can be found in previous works, e.g., see Borkowski et al. (2006); Williams et al. (2006); Dwek et al. (2008).) We assume that dust grains with characteristics of the above equilibrium model are continuously injected into shocked gas. After being injected, they are destroyed by thermal and non-thermal sputtering with ions and the grain size distribution is modified. (We neglect grain-grain shattering which is important for slow radiative shocks.) The erosion rates (da/dt) by sputtering depends on the chemical composition and temperature of the shocked gas as well as the speed of grains through the plasma (e.g., Nozawa et al. 2006). We adopt $da/dt = -1.6 \times 10^{-6} n_{\text{H}}$ and $-4.0 \times 10^{-6} n_{\text{H}} \mu\text{m yr}^{-1}$ for graphite and silicate grains, respectively. These constant erosion rates are good within about 50% for the temperature range of our sample SNRs, i.e., between 2×10^6 K and 2×10^7 K (Table 2). The gas density and temperature behind the shock front are assumed to remain the same. We calculated the cooling function of a fluid element and obtained a volume-averaged cooling rate by integrating it. For the X-ray cooling, it is necessary to incorporate the increase of the heavy element abundance of shocked gas with time owing to dust destruction and the different τ_{ion} that they experience, but we have found that the flux obtained by assuming a single τ_{ion} gives a satisfactory result. Figures 5-(a) and (b) show the resulting dust and X-ray cooling functions, respectively. The dust cooling function starts to deviate from the non-destruction case at $\tau_{\text{ion}} \gtrsim 10^{11} \text{ cm}^{-3} \text{ s}$, while the X-ray cooling function is much lower or higher than the CIE curve initially but approaches to it at $\tau_{\text{ion}} \gtrsim 10^{12} \text{ cm}^{-3} \text{ s}$. The resulting time-dependent $R_{\text{IRX, coll}}$ curves are shown as solid lines in Figure 4-(b). $R_{\text{IRX, coll}}$ fluctuates about the equilibrium ratio initially, but it steadily decreases as a result of dust destruction. As τ_{ion} increases from 10^{10} to $10^{13} \text{ cm}^{-3} \text{ s}$, $R_{\text{IRX, coll}}$ decreases in general at $T_e \lesssim 10^7$ K. Therefore, the scatter of the observed IRX flux ratio in Figure 4-(b) appears to be attributable to an evolutionary effect.

The τ_{ion} values of SNRs derived from the X-ray spectral analysis, however, are mostly $10^{11} \text{ cm}^{-3} \text{ s}$ except for the MM SNRs (Table 2) whereas, if we exclude the SNRs with high negative r_{50} , most SNRs excluding the young SNRs appear to lie between the two curves of $\tau_{\text{ion}} = 10^{11}$ and $10^{13} \text{ cm}^{-3} \text{ s}$ in Figure 4-(b). This inconsistency can be also seen in Figure 6 where we plot $R_{\text{IRX, obs}}$ versus τ_{ion} of SNRs. If we exclude the SNRs with high negative r_{50} , which are well above the theoretical curves, the SNRs are all below the theoretical curve and there appears to be no obvious correlation between $R_{\text{IRX, obs}}$ and τ_{ion} . Hence, the scatter in Figure 4 may be partly due to an evolutionary effect, but not entirely. We have derived $R_{\text{IRX, coll}}$ values for the individual SNRs from their τ_{ion} and T_e in Table 2, and the results are listed in Table 3. Figure 7 shows that the SNRs with negative r_{50} have $R_{\text{IRX, obs}} > R_{\text{IRX, coll}}$, whereas most other SNRs have $R_{\text{IRX, obs}} \lesssim R_{\text{IRX, coll}}$. In conclusion, only for a small number of SNRs are the $R_{\text{IRX, obs}}$ values consistent with that of hot plasma where dust grains are collisionally heated.

4. Discussion

In this section, we first consider possible physical explanations for the SNRs with $R_{\text{IRX,obs}}$ lower or higher than $R_{\text{IRX,coll}}$ (hereafter referred to as SNRs with low and high IRX flux ratios). We then discuss the implication on recent results from the LMC SNRs.

4.1. Supernova Remnants with Low IRX Flux Ratios

Among the SNRs with low $R_{\text{IRX,obs}}$ values, the most prominent are Kepler, Cas A, Tycho, and 3C397. These remnants deviate from the $R_{\text{IRX,coll}}$ curve by an order of magnitude in Figure 7. The first three are young historical SNRs, and their small $R_{\text{IRX,obs}}$ values might be due to additional X-ray emission. In Cas A and Tycho, the X-ray emission is dominated by the X-ray emission from SN ejecta and not by thermal emission from shocked surrounding gas (Hwang & Laming 2012; Hwang & Gotthelf 1997). In Kepler, the X-ray emission from the circumstellar medium is not negligible (Burkey et al. 2013). We estimate that $\geq 50\%$ of the X-ray flux is from SN ejecta from its soft band (0.3–0.7keV) image. It is interesting that these SNRs do have high positive r_{50} because the IR and X-ray emissions originate from spatially distinct regions unless the SNR contains a large amount of newly-formed SN dust such as Cas A. However, such positional shifts between the IR and X-ray sources are small and not apparent in their r_{50} . The nature of another prominent SNR 3C397 is uncertain. It had been proposed to be a middle-aged ($\sim 5,300$ yr) MM SNR evolving in a molecular cloud (Safi-Harb et al. 2005). CO observation revealed a large molecular cloud along the sight line toward 3C397 (Jiang et al. 2010), although there is no direct evidence (e.g., H_2 emission) for the interaction. However, its hard X-ray emission is dominated by SN ejecta, and it has been proposed that 3C397 is a young Type Ia SNR evolving in a medium of low ($\sim 1.6 \text{ cm}^{-3}$) density (Yamaguchi et al. 2015). The location of 3C397 in Figure 7 is very different from those of the other evolved MM SNRs that have high IRX flux ratios, and our result seems to support the latter interpretation, i.e., a young type Ia SNR where the X-ray emission inside the SNR is largely from SN ejecta. However, the X-ray absorbing column is large ($3 \times 10^{22} \text{ cm}^{-2}$) and there is a nearby HII region northwest of the remnant (3C397W; Dyer & Reynolds 1999) which is bright in infrared (see Fig. 1), so this conclusion needs to be confirmed by further studies.

There are two other MM SNRs with small $R_{\text{IRX,obs}}$ values: G292.0+1.8 and 3C396. G292.0+1.8 has significant X-ray emission from SN ejecta (Park et al. 2004), which explains its small $R_{\text{IRX,obs}}$ value. Note that it has $r_{50}(= 0.47)$ very different from other MM SNRs. For 3C396, we have not found a plausible explanation. Its X-ray emission is partly non-thermal, but its contribution to the soft X-ray flux appears to be negligible (Harrus & Slane 1999).

The other SNRs with considerably small $R_{\text{IRX,obs}}$ values are G15.9+0.2, Kes 75, Puppis A, and RCW 86. These SNRs have large r_{50} and thus the FIR emission is thought to be mainly from collisionally-heated dust. Their $R_{\text{IRX,obs}}$ values, however, are smaller than those of $R_{\text{IRX,coll}}$ by a factor of 2–5. (Note that we have excluded the X-ray emission from the central pulsar and

the pulsar wind nebula in Kes 75.) A possible explanation for this difference is that the DGR values in the surrounding media of these SNRs are lower than that of the general ISM (Arendt et al. 2010; Williams et al. 2011). Indeed, a similar conclusion has been reached for other Galactic and Magellanic SNRs in previous studies (Blair et al. 2007; Lee et al. 2009; Borkowski et al. 2006; Williams et al. 2006; Sankrit et al. 2010; Williams et al. 2011). Among the SNRs with large r_{50} , G11.2–0.3, Kes 73, the Cygnus Loop, and RCW 103 have $R_{\text{IRX,obs}}$ consistent with $R_{\text{IRX,coll}}$, which appears to indicate that the DGR in the ambient or circumstellar medium of these SNRs might be equal to that of the general ISM. It is, however, noteworthy that there could be some extra contribution to the IR emission, e.g., IR line and/or radiatively heated dust emission (see the next section). In the Cygnus Loop, for example, Braun & Strom (1986) estimated that about 25% of the IRAS 60 μm emission is from the dust in recombined gas in the postshock layer. From their analysis of a non-radiative shock in the Cygnus Loop, Sankrit et al. (2010) concluded that the DGR in the ambient medium is about half that of the general ISM. Therefore, it is not impossible that these SNRs do also have DGR values somewhat below that of the general ISM.

4.2. Supernova Remnants with High IRX Flux Ratios

All the SNRs with $R_{\text{IRX,obs}}$ values significantly larger than those of $R_{\text{IRX,coll}}$ are MM SNRs with large negative r_{50} , e.g., W44, W49B, 3C391, IC 443, Kes 17, and G349.7+0.2. The $R_{\text{IRX,obs}}$ values of some of these SNRs are greater than those of $R_{\text{IRX,coll}}$ by almost by an order of magnitude. The FIR emission in these SNRs is not correlated with X-rays, and therefore is probably not from collisionally heated dust grains. There could be some contribution from ionic lines to the observed IR flux, but, as we discussed in § 2.1, it is considered to be less than a few tens of percent. Another distinct property of these SNRs indicating a different origin of the FIR emission is their low dust temperatures (Figure 8; see also Table 1). These SNRs have $T_d = 43\text{--}51$ K whereas most other SNRs have $T_d = 57\text{--}67$ K except for the young SNRs Kepler and Cas A. For collisionally heated dust in hot ($\gtrsim 10^7$ K) plasma, dust temperature is mainly determined by electron density (n_e), and, for a typical electron density of $n_e = 1 \text{ cm}^{-3}$ and silicate grains of radius $0.01\text{--}0.1 \mu\text{m}$, $T_d = 60\text{--}50$ K (Dwek et al. 2008). Therefore, dust temperatures of $57\text{--}67$ K are consistent with the FIR emission being largely from collisionally-heated dust grains of radius $\lesssim 0.01 \mu\text{m}$, but $43\text{--}51$ K might be rather low. In Figure 8, there appears to be a weak correlation (correlation coefficient = 0.6) between $R_{\text{IRX,obs}}$ and T_d , and if we naively perform a least-squares fitting excluding the SNRs with low $R_{\text{IRX,obs}}$ values in Figure 7, we obtain

$$\log_{10} R_{\text{IRX,obs}} = -0.078(0.007)T_d + 5.50(0.40), \quad (4)$$

where the dust temperature (T_d) is in K. If dust grains are heated by collisions in hot plasma, then we do not expect such a correlation because T_d is mainly determined by n_e whereas the IRX flux ratio is independent of n_e . Instead, the apparent correlation in Figure 8 might represent different origins for the dust IR emissions at low and ‘high’ temperatures.

The low dust temperature and large $R_{\text{IRX,obs}}$ values of the MM SNRs with large negative r_{50} in Figure 8 probably indicate that the FIR emission in these SNRs is largely from dust heated by shock radiation. All these SNRs, e.g., W44 (Reach et al. 2005), W49B (Keohane et al. 2007), IC 443 (Lee et al. 2012), Kes 17 (Lee et al. 2011), and G349.7+0.2 (Lazendic et al. 2010), are indeed known to be interacting with dense ambient medium and the shock is largely radiative. In a radiative shock, essentially all the shock energy is converted into UV and X-ray radiation. This UV and X-ray radiation from the hot shocked gas ionizes and heats the surrounding gas to produce an extended temperature plateau region in the postshock cooling layer and also a ‘radiative precursor’ in the preshock gas, both of which are at $T_e \sim 10^4$ K (see, for example, Shull & McKee (1979); Hollenbach & McKee (1979); Draine & McKee (1993) for the structure of radiative shock). Since at shock speeds $\lesssim 200$ km s $^{-1}$, dust grains are mostly not destroyed although their size distribution may be modified by grain-grain shattering (Jones et al. 1996), we expect dust grains in these hot and warm regions that will be mainly heated by attenuated X-ray and UV radiation and also by the recombination radiation from the ionized gas in those regions (Hollenbach & McKee 1979; Andersen et al. 2011; Lee et al. 2011; Koo 2014). If there are enough gas and dust columns beyond these hot and warm regions, the dust IR emission could be further absorbed by cold dust and re-emitted at longer wavelengths. Therefore, we expect that, in these SNRs, a significant fraction of the shock energy might be converted into IR radiation of a broad spectral energy distribution at color temperature considerably lower than that of the collisionally heated dust.

It would be interesting to determine what fraction of shock energy is converted into the IR emission in these SNRs. We define the characteristic efficiency of converting shock energy into IR radiation (ϵ_{IR}) for an SNR by the following equation

$$L_{\text{IR}} = \frac{1}{2} \epsilon_{\text{IR}} n_a \mu_{\text{H}} v_s^3 \times 4\pi R_s^2 = 3.7 \times 10^4 \epsilon_{\text{IR}} n_{a,1} v_{s,2}^3 R_{s,1}^2 L_{\odot} \quad (5)$$

where L_{IR} is the IR luminosity, n_a is the hydrogen nuclei number density of the ambient medium, v_s and R_s are the shock speed and radius of the SNR, and $\mu_{\text{H}} = 2.34 \times 10^{-24}$ g is the mean mass per hydrogen nucleus for a gas of cosmic abundance. In the second equation, we normalized the parameters by their typical values, i.e., $n_{a,1} \equiv n_a/(10 \text{ cm}^{-3})$, $v_{s,2} \equiv v_s/(10^2 \text{ km s}^{-1})$, and $R_{s,1} \equiv R_s/(10 \text{ pc})$. Note that $\frac{1}{2} n_a \mu_{\text{H}} v_s^3$ is the incoming energy flux, so ϵ_{IR} would be the ratio of IR luminosity to the energy incoming rate for a spherically symmetric SNR of radius R_s in a uniform medium with a density of n_a . Of course real SNRs are not spherically symmetric, and n_a and v_s usually vary over the remnant. For radiative portion of the SNRs, we expect $n_a \gtrsim 1 \text{ cm}^{-3}$ and $v_s \lesssim 200 \text{ km s}^{-1}$, so the cooling time, $\tau_{\text{cool}} \approx 3.8 \times 10^3 v_{s,2}^{3.4}/n_a$ yr (Draine 2011), becomes shorter than the age of the SNR. We may obtain a constraint on n_a and v_s from X-ray observation by assuming that there is a pressure equilibrium between the shock pressure and the thermal pressure of the X-ray emitting gas, i.e., $n_a \mu_{\text{H}} v_s^2 \approx 1.9 n_e k_B T_e$ where n_e and T_e are the electron density and temperature of hot gas, respectively. (We assume fully ionized gas with $n(\text{He})/n(\text{H}) = 0.1$.) The shock speed then is given by

$$v_{s,2} \approx 1.06 n_{a,1}^{-0.5} (n_e \sqrt{f_V T_7})^{0.5} f_V^{-0.25}, \quad (6)$$

where f_V is the volume filling factor of the X-ray emitting gas and $T_7 \equiv (T_e/10^7 \text{ K})$. Note that we used $n_e\sqrt{f_V}$ (instead of n_e) because it is the parameter obtained from X-ray observation, e.g., X-ray flux is proportional to $\int n_e^2 dV = n_e^2 f_V (4\pi/3) R_s^3$. If we substitute this shock speed into Equation (5), the IR luminosity is given by

$$L_{\text{IR}} = 4.4 \times 10^4 \epsilon_{\text{IR}} n_{a,1}^{-0.5} n_e \sqrt{f_V} T_7^{1.5} f_V^{-0.75} R_{s,1}^2 L_{\odot} \quad (7)$$

In the above equation, L_{IR} is from the IR observation (Table 1) and $n_e\sqrt{f_V}$ and T_7 are from the X-ray observation (Table 2), so that if we know f_V and n_a we can determine ϵ_{IR} (assuming that we know the distance to the SNR and therefore R_s).

Table 4 summarizes the physical parameters of six SNRs with high IRX ratios and their ϵ_{IR} . We fixed $f_V = 0.5$ because the volume filling factors are uncertain, although it has been estimated for some SNRs, e.g., 0.36 (W49B; Kawasaki et al. 2005) and ~ 0.4 (IC 443; Troja et al. 2006). The ambient density is also uncertain. Chevalier (1999) showed that some of these SNRs, i.e., W44, IC 443, and 3C391, are well described by an SNR model expanding within a molecular cloud with an interclump density of 5–25 cm^{-3} , while Park et al. (2013) derived a somewhat lower density (1.9 cm^{-3}) for W44 from H α 21 cm line observations (see also Koo & Heiles 1995). We adopted 3–15 cm^{-3} for n_a (see note in Table 4). It is not unusual to observe both atomic and molecular shocks in these SNRs, so the n_a values in Table 4 should be considered as reference values. Note that we can scale the result using $\epsilon_{\text{IR}} \propto n_a^{0.5} f_V^{0.75}$ (Equation 7). Although there are considerable uncertainties in ϵ_{IR} for a particular SNR, our result shows that $\epsilon_{\text{IR}} \gtrsim 30\%$ in general. We can imagine that this ‘global’ efficiency ϵ_{IR} will be proportional to the fraction of surface area encountering dense ambient medium and thus the local efficiency of converting shock energy into IR radiation could be higher. For comparison, the fraction of shock energy that goes into the collisional-heating of dust is 1%–10% for shocks with speeds of 100–200 km s^{-1} (Draine 1981). Therefore, as we expect from their large IRX flux ratios, the IR luminosities of these SNRs are significantly greater than those from collisionally-heated dust.

4.3. LMC Supernova Remnants with High and Low IRX Flux Ratios

Recently Seok et al. (2015) conducted a systematic study of the LMC SNRs using *Spitzer* and *Chandra* data, and showed that the IRX flux ratios of the LMC SNRs are systematically lower than those of the Galactic SNRs, which is consistent with the low DGR and the low metallicity of the LMC, i.e., the dust cooling rate is proportional to the DGR which is one-fourth of the Galactic value while the gas cooling rate is proportional to metallicity which is one-half of the Galactic value. They further classified the SNRs into three groups, i.e., SNRs with definite, partial, and lack of IRX correlation, and found that the IRX flux ratios of the SNRs with a partial or lack of IRX morphological correlation are systematically higher than the ones with definite correlation.

In Figure 9, we plot the $R_{\text{IRX,obs}}$ values of the LMC SNRs against their dust temperatures. The IRX flux ratios are from Seok et al. (2015) while dust temperatures are derived here from the 24

and $70\ \mu\text{m}$ fluxes in Seok et al. (2013). We can see that the SNRs with a lack of IRX morphological correlation not only have large $R_{\text{IRX,obs}}$ values but also have low temperatures as we have found for the Galactic SNRs. Their temperature ranges from 45 to 56 K, the maximum of which is a little higher than the 51 K of the Galactic SNRs. However, the dust temperature of the SNRs with definite IRX morphological correlation extends over a broad range from 48 to 80 K (excluding 1987A, for which T_d is 166 K). There is one SNR (0453–68.5) with a definite correlation that has an exceptionally low (~ 49 K) dust temperature. Williams et al. (2006) derived a comparable dust temperature (40–55 K) for the northern shell of this SNR. Its low T_d could be due to low electron density combined with low electron temperature, e.g., $0.76\ \text{cm}^{-3}$ and $0.29\ \text{keV}$ (Williams et al. 2006). Figure 9 also shows that about two-thirds of the LMC SNRs are below the dashed line, which confirms the conclusion of Seok et al. (2015) that the IRX flux ratio of the LMC SNRs are systematically lower than those of the Galactic SNRs. (Note that Seok et al. (2015) used the X-ray flux from the Chandra SNR catalog, so that their IRX flux ratios are different from ours.) In Figure 9, however, the SNRs at low and high dust temperatures are not necessarily below the dashed line. This may be because, as we have found in the Galactic SNRs, the IR emission of the SNRs at low temperatures is dominated by radiatively-heated dust grains while the X-ray emission of the SNRs at high temperatures is dominated by SN ejecta, so that the low DGR and the low metallicity do not explicitly appear in the IRX flux ratio. Indeed the SNRs with high dust temperatures, i.e., N132D, N103B, 0519–69.0, and 0509–67.5, are all the youngest ($\lesssim 3,000$ yr) SNRs in the LMC. In conclusion, the location of SNRs in the $(R_{\text{IRX,obs}}, T_d)$ diagram reflects the SNR environment as well as their natural properties.

5. Summary and Conclusion

FIR dust emission is a dominant emission for SNRs, and it has been pointed out that FIR cooling by collisionally-heated dust could be more important than the X-ray cooling by hot gas in SNRs over most of their lifetimes. With the development of IR astronomy, this was confirmed by comparing the IR to X-ray fluxes. The observed IRX flux ratios $R_{\text{IRX,obs}}$ however, scatter over three orders of magnitudes, and with the *IRAS* data of several arcminute resolution, it was difficult to explore the true nature of the IR emission for most SNRs. In this paper, we conducted a systematic study of the IR and X-ray properties of 20 SNRs using the data from recent space missions to reveal details of morphology. We first showed that SNRs have diverse relative IR and X-ray morphologies, from very similar to very different, and that their resemblance may be represented by the correlation parameter r_{50} (§ 2.3). We then have derived IRX flux ratios ($R_{\text{IRX,obs}}$) of the SNRs and found that there is a systematic dependence on r_{50} . By comparing $R_{\text{IRX,obs}}$ to the expected IRX flux ratios ($R_{\text{IRX,coll}}$) for hot plasma where dust grains are collisionally heated, we explored how the IRX flux ratios and IRX morphology are related to the SNR environment and their natural properties. We summarize our main results as follows:

1. The $R_{\text{IRX,obs}}$ values of SNRs range from 0.3 to 200. The SNRs with high negative r_{50} have

systematically higher IRX flux ratios.

2. The $R_{\text{IRX,obs}}$ values of all SNRs except a few are all below the expected ratio for hot, dusty plasma of constant DGR in collisional ionization equilibrium. This can be attributed to dust destruction and NEI gas cooling behind the shock front in some SNRs, but for most SNRs $R_{\text{IRX,obs}}$ values are either considerably larger or smaller than those of $R_{\text{IRX,coll}}$.

3. Among the SNRs with $R_{\text{IRX,obs}}$ values significantly less than those of $R_{\text{IRX,coll}}$, the most prominent are young SNRs such as Cas A, Kepler, and Tycho. In these SNRs, the X-ray emission is dominated by metal-rich SN ejecta and our $R_{\text{IRX,coll}}$ values are not applicable. We consider that this might be also the case for other young SNRs with anticorrelated IRX morphology in this category. There are, however, also SNRs without apparent X-ray emission from SN ejecta. They exhibit good IRX morphological correlation. For these SNRs, a low DGR of the ambient medium seems to be a plausible explanation.

4. All SNRs with $R_{\text{IRX,obs}}$ values significantly greater than $R_{\text{IRX,coll}}$ ones have large negative r_{50} , i.e., are with anticorrelated IRX morphology. The dust temperature of these SNRs is systematically lower than those of the other SNRs. These SNRs are known to be interacting with a dense environment, and the IR emission in these SNRs is probably from dust heated by shock radiation rather than by collisions. The global conversion efficiency of shock energy to IR emission is estimated to be more than a few tens of percent.

Our results show that the IRX flux ratios together with dust temperature are useful indicators for the SNR environment as well as their natural properties. We may infer that the SNRs with small $R_{\text{IRX,obs}}$ and high T_d values are young SNRs with X-ray emission dominated by SN ejecta, whereas the SNRs with large $R_{\text{IRX,obs}}$ and low T_d are evolved SNRs interacting with a dense environment. This was confirmed for the SNRs in the LMC. Such information might be particularly useful for the study of SNRs in galaxies where the SNRs are not resolved.

We thank the anonymous referee and Jeonghee Rho for their comments which helped to improve the manuscript. This research was supported by the Basic Science Research Program through the National Research Foundation of Korea(NRF) funded by the Ministry of Science, ICT and Future Planning (2014R1A2A2A01002811). H.-J. K. was supported by NRF(National Research Foundation of Korea) Grant funded by the Korean Government (NRF-2012-Fostering Core Leaders of the Future Basic Science Program). This work is based on observations made with the *Spitzer Space Telescope*, which is operated by the Jet Propulsion Laboratory, California Institute of Technology under a contract with NASA, data obtained from the *Chandra* Data Archive, and observations obtained with *XMM-Newton*, an ESA science mission with instruments and contributions directly funded by ESA Member States and NASA. This publication makes use of data products from the *Wide-field Infrared Survey Explorer*, which is a joint project of the University of California, Los Angeles, and the Jet Propulsion Laboratory/California Institute of Technology, funded by the National Aeronautics and Space Administration and the *ROSAT* Data Archive of

the Max-Planck-Institut für extraterrestrische Physik (MPE) at Garching, Germany.

REFERENCES

- Andersen, M., Rho, J., Reach, W. T., Hewitt, J. W., & Bernard, J. P. 2011, *ApJ*, 742, 7
- Arendt, R. G. 1989, *ApJS*, 70, 181
- Arendt, R. G., Dwek, E., Blair, W. P., et al. 2010, *ApJ*, 725, 585
- Arendt, R. G., Dwek, E., & Leisawitz, D. 1992, *ApJ*, 400, 562
- Asplund, M., Grevesse, N., Sauval, A. J., & Scott, P. 2009, *ARA&A*, 47, 481
- Barlow, M. J., Krause, O., Swinyard, B. M., et al. 2010, *A&A*, 518, L138
- Blair, W. P., Ghavamian, P., Long, K. S., et al. 2007, *ApJ*, 662, 998
- Borkowski, K. J., Williams, B. J., Reynolds, S. P., et al. 2006, *ApJ*, 642, L141
- Braun, R., & Strom, R. G. 1986, *A&A*, 164, 208
- Burkey, M. T., Reynolds, S. P., Borkowski, K. J., & Blondin, J. M. 2013, *ApJ*, 764, 63
- Burton, M., & Spyromilio, J. 1993, *Proceedings of the Astronomical Society of Australia*, 10, 327
- Carey, S. J., Noriega-Crespo, A., Mizuno, D. R., et al. 2009, *PASP*, 121, 76
- Cassam-Chenaï, G., Hughes, J. P., Ballet, J., & Decourchelle, A. 2007, *ApJ*, 665, 315
- Chen, Y., Su, Y., Slane, P. O., & Wang, Q. D. 2004, *ApJ*, 616, 885
- Chevalier, R. A. 1999, *ApJ*, 511, 798
- Cox, D. P., & Raymond, J. C. 1985, *ApJ*, 298, 651
- Cox, D. P., Shelton, R. L., Maciejewski, W., et al. 1999, *ApJ*, 524, 179
- Draine, B. T. 1981, *ApJ*, 245, 880
- Draine, B. T. 2011, *Physics of the Interstellar and Intergalactic Medium* (Princeton, NJ: Princeton Univ. Press)
- Draine, B. T., & McKee, C. F. 1993, *ARA&A*, 31, 373
- Draine, B. T., & Salpeter, E. E. 1979, *ApJ*, 231, 438
- Dubner, G., Loiseau, N., Rodríguez-Pascual, P., et al. 2013, *A&A*, 555, A9

- Dwek, E. 1981, *ApJ*, 247, 614
- Dwek, E. 1987, *ApJ*, 322, 812
- Dwek, E., Arendt, R. G., Bouchet, P., et al. 2008, *ApJ*, 676, 1029
- Dwek, E., Petre, R., Szymkowiak, A., & Rice, W. L. 1987, *ApJ*, 320, L27
- Dyer, K. K., & Reynolds, S. P. 1999, *ApJ*, 526, 365
- Ferland, G. J., Porter, R. L., van Hoof, P. A. M., et al. 2013, *Rev. Mexicana Astron. Astrofis.*, 49, 137
- Gelfand, J. D., Castro, D., Slane, P. O., et al. 2013, *ApJ*, 777, 148
- Gomez, H. L., Clark, C. J. R., Nozawa, T., et al. 2012, *MNRAS*, 420, 3557
- Graham, J. R., Evans, A., Albinson, J. S., Bode, M. F., & Meikle, W. P. S. 1987, *ApJ*, 319, 126
- Green, D. A. 2014, *Bulletin of the Astronomical Society of India*, 42, 47
- Harrus, I. M., Hughes, J. P., Singh, K. P., Koyama, K., & Asaoka, I. 1997, *ApJ*, 488, 781
- Harrus, I. M., & Slane, P. O. 1999, *ApJ*, 516, 811
- Helfand, D. J., Collins, B. F., & Gotthelf, E. V. 2003, *ApJ*, 582, 783
- Hines, D. C., Rieke, G. H., Gordon, K. D., et al. 2004, *ApJS*, 154, 290
- Hollenbach, D., & McKee, C. F. 1979, *ApJS*, 41, 555
- Hollenbach, D., & McKee, C. F. 1989, *ApJ*, 342, 306
- Hwang, U., & Gotthelf, E. V. 1997, *ApJ*, 475, 665
- Hwang, U., & Laming, J. M. 2012, *ApJ*, 746, 130
- Hwang, U., Petre, R., & Flanagan, K. A. 2008, *ApJ*, 676, 378
- Jeong, I.-G., Koo, B.-C., & Lee, H.-G. 2012, *Publication of Korean Astronomical Society*, 27, 235
- Jiang, B., Chen, Y., Wang, J., et al. 2010, *ApJ*, 712, 1147
- Jones, A. P., Tielens, A. G. G. M., & Hollenbach, D. J. 1996, *ApJ*, 469, 740
- Kawasaki, M., Ozaki, M., Nagase, F., Inoue, H., & Petre, R. 2005, *ApJ*, 631, 935
- Keohane, J. W., Reach, W. T., Rho, J., & Jarrett, T. H. 2007, *ApJ*, 654, 938
- Koo, B.-C. 2014, *IAU Symposium*, 296, 214

- Koo, B.-C., & Heiles, C. 1995, *ApJ*, 442, 679
- Ku, W. H.-M., Kahn, S. M., Pisarski, R., & Long, K. S. 1984, *ApJ*, 278, 615
- Landi, E., Del Zanna, G., Young, P. R., Dere, K. P., & Mason, H. E. 2012, *ApJ*, 744, 99
- Lazendic, J. S., Slane, P. O., Hughes, J. P., Chen, Y., & Dame, T. M. 2005, *ApJ*, 618, 733
- Lazendic, J. S., Wardle, M., Whiteoak, J. B., Burton, M. G., & Green, A. J. 2010, *MNRAS*, 409, 371
- Lee, H.-G., Koo, B.-C., Moon, D.-S., et al. 2009, *ApJ*, 706, 441
- Lee, J.-J., Koo, B.-C., Snell, R. L., et al. 2012, *ApJ*, 749, 34
- Lee, H.-G., Moon, D.-S., Koo, B.-C., et al. 2011, *ApJ*, 740, 31
- Lee, J.-J., Park, S., Hughes, J. P., et al. 2010, *ApJ*, 711, 861
- Lee, J.-J., Park, S., Hughes, J. P., & Slane, P. O. 2014, *ApJ*, 789, 7
- Mathis, J. S., Rumpl, W., & Nordsieck, K. H. 1977, *ApJ*, 217, 425
- Molinari, S., Swinyard, B., Bally, J., et al. 2010, *PASP*, 122, 314
- Noriega-Crespo, A., Hines, D. C., Gordon, K., et al. 2009, *The Evolving ISM in the Milky Way and Nearby Galaxies*, 46
- Nozawa, T., Kozasa, T., & Habe, A. 2006, *ApJ*, 648, 435
- Ostriker, J., & Silk, J. 1973, *ApJ*, 184, L113
- Park, G., Koo, B.-C., Gibson, S. J., et al. 2013, *ApJ*, 777, 14
- Park, S., Hughes, J. P., Slane, P. O., et al. 2004, *ApJ*, 602, L33
- Pinheiro Gonçalves, D., Noriega-Crespo, A., Paladini, R., Martin, P. G., & Carey, S. J. 2011, *AJ*, 142, 47
- Reach, W. T., Rho, J., & Jarrett, T. H. 2005, *ApJ*, 618, 297
- Raymond, J. C. 1979, *ApJS*, 39, 1
- Reynolds, S. P., Borkowski, K. J., Hwang, U., et al. 2006, *ApJ*, 652, L45
- Rho, J. 1995, Ph.D. Thesis (Univ. of Maryland, College Park)
- Rho, J., & Petre, R. 1998, *ApJ*, 503, L167
- Safi-Harb, S., Dubner, G., Petre, R., Holt, S. S., & Durouchoux, P. 2005, *ApJ*, 618, 321

- Saken, J. M., Fesen, R. A., & Shull, J. M. 1992, *ApJS*, 81, 715
- Sankrit, R., Williams, B. J., Borkowski, K. J., et al. 2010, *ApJ*, 712, 1092
- Seok, J. Y., Koo, B.-C., & Hirashita, H. 2015, *ApJ*, submitted
- Seok, J. Y., Koo, B.-C., & Onaka, T. 2013, *ApJ*, 779, 134
- Shull, J. M., & McKee, C. F. 1979, *ApJ*, 227, 131
- Sibthorpe, B., Ade, P. A. R., Bock, J. J., et al. 2010, *ApJ*, 719, 1553
- Troja, E., Bocchino, F., & Reale, F. 2006, *ApJ*, 649, 258
- Tsunemi, H., Katsuda, S., Nemes, N., & Miller, E. D. 2007, *ApJ*, 671, 1717
- Vink, J. 2012, *A&A Rev.*, 20, 49
- Weingartner, J. C., & Draine, B. T. 2001, *ApJ*, 548, 296
- White, R. L., & Long, K. S. 1991, *ApJ*, 373, 543
- Williams, B. J., Borkowski, K. J., Reynolds, S. P., et al. 2006, *ApJ*, 652, L33
- Williams, B. J., Blair, W. P., Blondin, J. M., et al. 2011, *ApJ*, 741, 96
- Williams, B. J., Borkowski, K. J., Reynolds, S. P., et al. 2011, *ApJ*, 729, 65
- Yamaguchi, H., Badenes, C., Foster, A. R., et al. 2015, *ApJ*, 801, L31

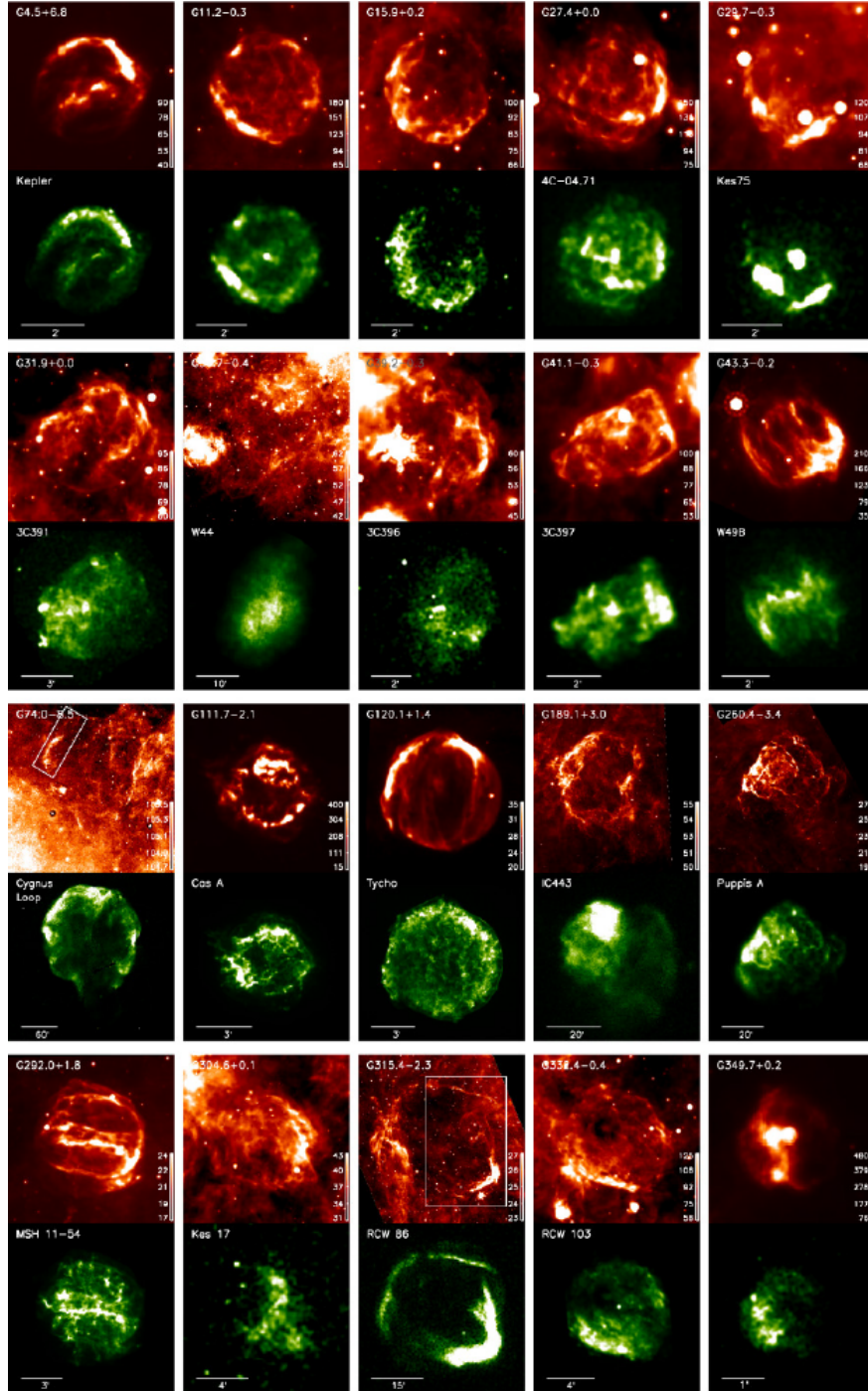


Fig. 1.— IR and X-ray images of the 20 SNRs in Table 1. Red images in upper rows are *Spitzer* 24 μm images; green images in lower rows are *Chandra* 0.3–2.1 keV images from the *Chandra* SNR catalog (<http://hea-www.cfa.harvard.edu/ChandraSNR/>) except for the following: IR image of Cygnus Loop is a *Wide-Field Infrared Survey Explorer* 22 μm image; X-ray images of Cygnus Loop, IC 443, and Puppis A are *ROSAT* PSPC 0.1–2.4 keV images, and X-ray images of Kes 17 and RCW 86 are *XMM-Newton* images. The color intensity scale is linear in both IR and X-ray images. The white boxes in some SNR images represent areas where the correlation coefficient between IR and X-ray intensities in § 2.3 are derived.

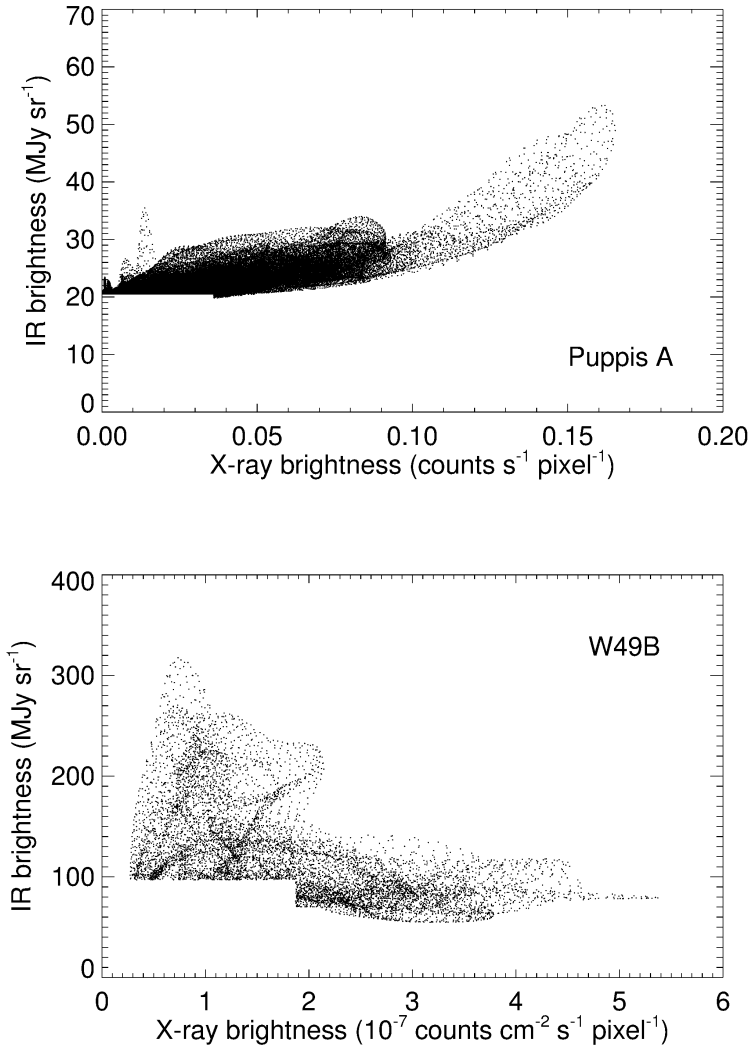


Fig. 2.— Scattered diagrams of 24 μm versus X-ray brightness for Puppis A (upper frame) and W49B (lower frame) that have the largest positive (0.76) and the largest negative (-0.49) correlation coefficient r_{50} , respectively.

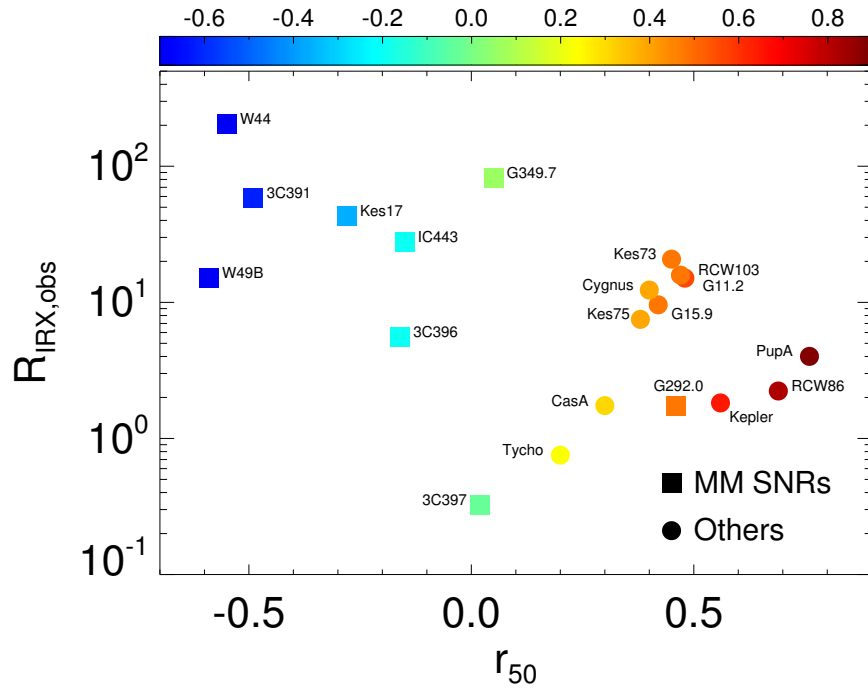


Fig. 3.— Observed IRX flux ratio versus r_{50} . The color of SNR symbols varies from blue to red with r_{50} increasing from -0.7 to 0.9 as in the color bar. The square symbol indicates that the SNR is an MM-type SNR.

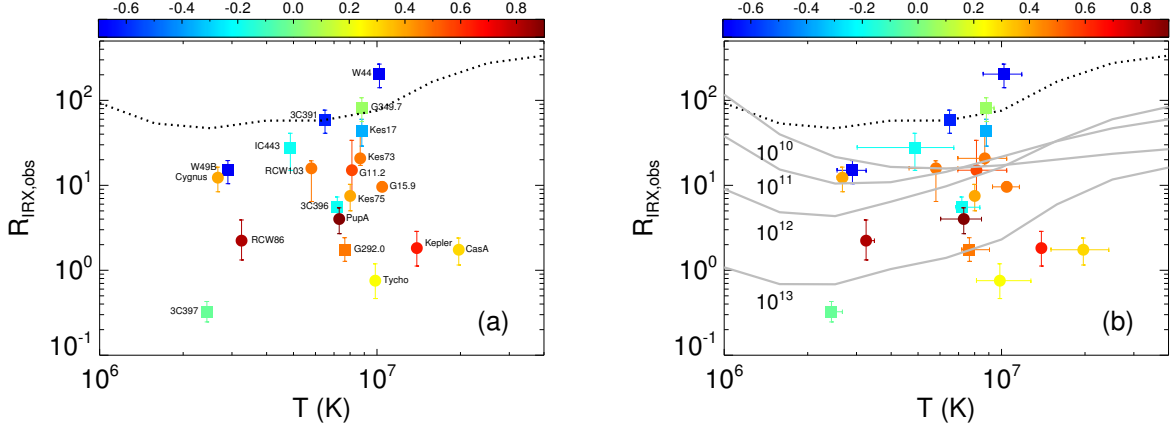


Fig. 4.— (a) Observed IRX flux ratio versus temperature of X-ray emitting plasma. The dotted line is a theoretical curve representing the IRX flux ratio of hot plasma in thermal and collisional ionization equilibrium. The colors and symbols are the same as in Figure 3. (b) Same as (a) but with time-dependent theoretical curves overlaid. The solid curves represent the IRX flux ratios for hot plasma at $\tau_{\text{ion}} = 10^{10}, 10^{11}, 10^{12}$, and 10^{13} cm^{-3} s after being shocked (see text for details).

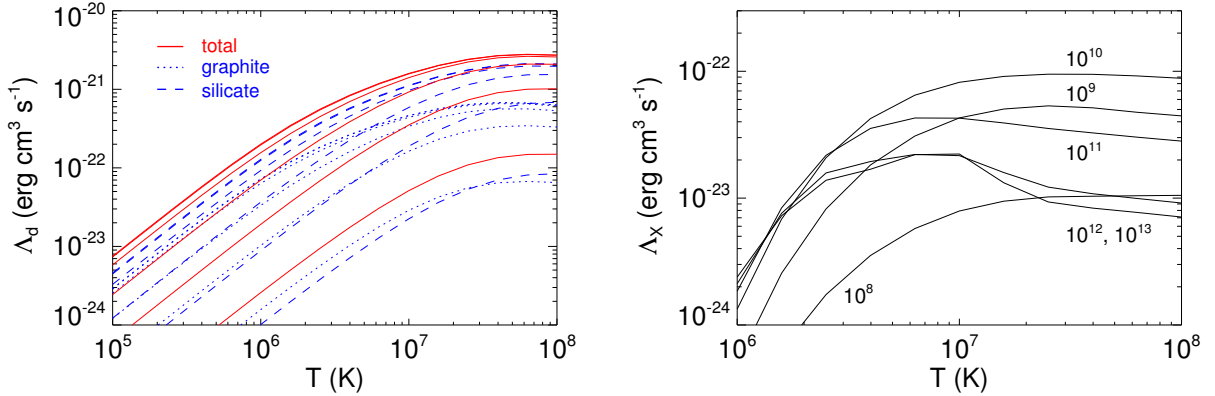


Fig. 5.— (Left) Time-dependent dust cooling function of shocked gas at $\tau_{\text{ion}} = 10^8, 10^9, 10^{10}, 10^{11}$, and 10^{12} cm^{-3} s from top to bottom. (Right) Time-dependent NEI X-ray (0.3–2.1 keV) cooling function. The curves are labeled by τ_{ion} (cm^{-3} s).

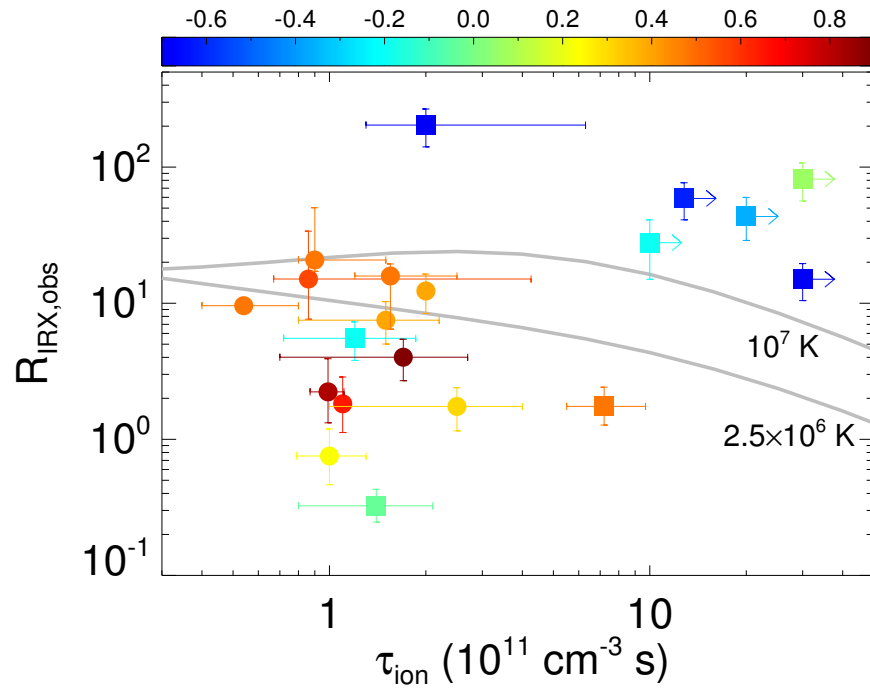


Fig. 6.— Observed IRX flux ratio versus ionization timescale. Solid curves are theoretical curves for hot plasma at $T_e = 10^7 \text{ K}$ and $2.5 \times 10^6 \text{ K}$. The colors and symbols are the same as in Figure 3.

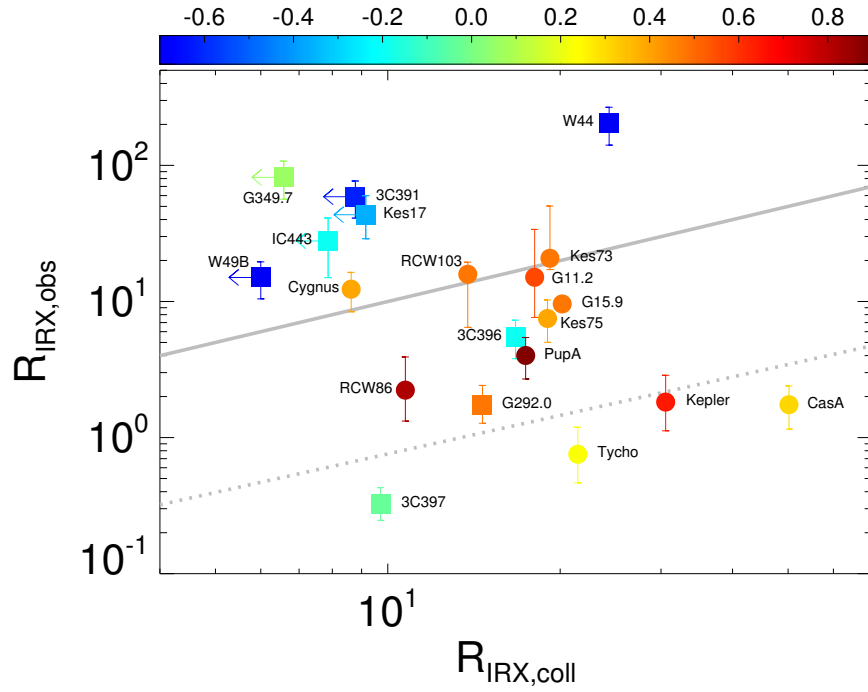


Fig. 7.— Observed IRX flux ratio versus theoretical IRX flux ratio for hot plasma where dust grains are heated by collisions. The solid and dotted curves represent when $R_{\text{IRX,obs}} = R_{\text{IRX,coll}}$ and $0.1R_{\text{IRX,coll}}$, respectively. The errors in $R_{\text{IRX,coll}}$ are not shown but may be found in Table 3. The colors and symbols are the same as in Figure 3.

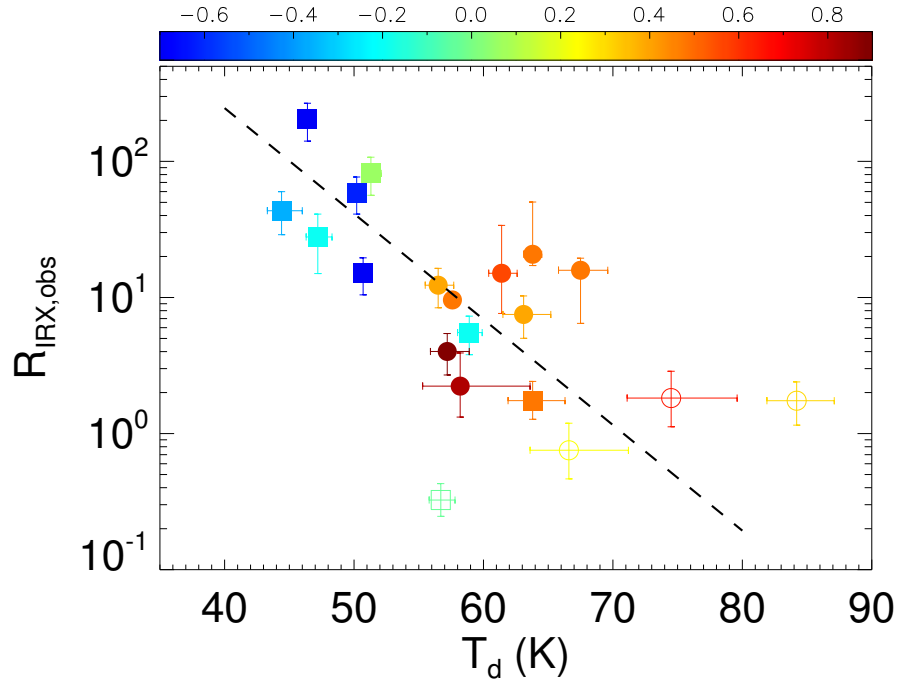


Fig. 8.— Observed IRX flux ratio versus dust temperature T_d . The dashed line is the best-fit curve obtained by least-squares fitting (Equation 4). The empty circles represent the SNRs with low $R_{\text{IRX,obs}}$ values in Figure 7, which are excluded in the fit. The colors and the other symbols are the same as in Figure 3.

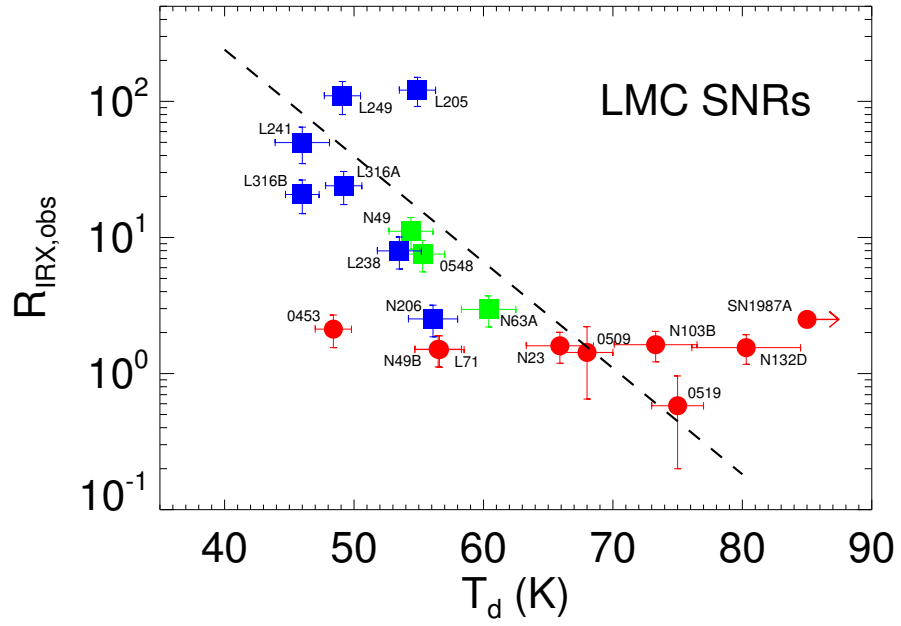


Fig. 9.— Observed IRX flux ratio versus dust temperature T_d for the SNRs in the LMC. The red circle, green box, and blue box symbols represent the SNRs with definite (red circle), partial (green box), and lack of (blue box) IRX morphological correlation, respectively. The dashed line is the best-fit curve for the Galactic SNRs in Figure 8.

Table 1. Infrared Fluxes and Dust Temperatures of 20 SNRs.

SNR	Other Name	F_{24} (Jy)	F_{70} (Jy)	T_d (K)	F_{IR} (10^{-9} ergs cm $^{-2}$ s $^{-1}$)	Reference
G4.5+6.8	Kepler	9.50 (1.0)	10.2 (2.7)	75.0 (-3.5,+5.2)	1.83 (-0.45,+0.91)	1
G11.2-0.3	...	38.6 (1.5)	124.7 (14.0)	61.6 (-1.1,+1.2)	12.8 (-1.3,+ 1.6)	This work
G15.9+0.2	...	10.1 (0.4)	49.1 (2.7)	57.8 (-0.5,+0.6)	4.32 (-0.24,+0.27)	This work
G27.4+0.0	Kes 73	30.1 (1.2)	76.6 (4.1)	64.1 (-0.7,+0.7)	8.73 (-0.53,+0.61)	This work
G29.7-0.3	Kes 75	10.2 (0.4)	27.9 (4.9)	63.3 (-1.6,+2.1)	3.08 (-0.45,+0.66)	This work
G31.9+0.0	3C391	33.9 (1.4)	434.9 (21.9)	50.3 (-0.4,+0.4)	28.6 (-1.3,+ 1.5)	This work
G34.7-0.4	W44	94.4 (9.5)	2243. (114.)	46.5 (-0.6,+0.7)	129.2 (-9.2,+11.3)	This work
G39.2-0.3	3C396	6.4 (0.6)	26.8 (1.6)	59.1 (-0.9,+1.1)	2.49 (-0.22,+0.28)	This work
G41.1-0.3	3C397	18.8 (0.8)	101.4 (11.9)	56.9 (-0.9,+1.1)	8.60 (-0.82,+1.06)	This work
G43.3-0.2	W49B	62.8 (2.5)	750. (38.)	50.8 (-0.4,+0.4)	50.2 (-2.3,+ 2.6)	This work
G74.0-8.5	Cygnus Loop	172. (17.)	1430. (140.)	47.5 (-1.3,+1.7)	85.3 (-12.6,+20.4)	2
G111.7-2.1	Cas A	202. (20.)	120. (12.)	85.0 (-2.4,+3.0)	32.1 (-5.1,+ 7.3)	3, 4
G120.1+1.4	Tycho	19.5 (3.0)	38.5 (10.8)	66.9 (-3.0,+4.7)	4.94 (-1.20,+2.50)	1
G189.1+3.0	IC 443	68.8 (6.9)	1349. (202.)	47.6 (-0.9,+1.2)	80.7 (-8.9,+12.5)	This work
G260.4-3.4	Puppis A	187. (19.)	955. (143.)	56.8 (-1.3,+1.7)	82.9 (-10.8,+15.6)	This work
G292.0+1.8	MSH 11-54	12.0 (0.7)	30.6 (6.1)	64.0 (-1.9,+2.5)	3.48 (-0.58,+0.91)	5
G304.6+0.1	Kes 17	2.2 (0.4)	75. (15.)	44.4 (-1.1,+1.6)	4.08 (-0.59,+0.96)	6
G315.4-2.3	RCW 86	0.69 (0.19)	3.10 (1.06)	58.5 (-3.0,+5.5)	0.28 (-0.08,+0.20)	7
G332.4-0.4	RCW 103	75.0 (7.5)	137.0 (17.2)	67.9 (-1.7,+2.1)	18.3 (-2.6,+ 3.7)	This work
G349.7+0.2	...	39.6 (3.9)	435.0 (21.8)	51.4 (-0.7,+0.8)	29.8 (-2.3,+ 2.8)	This work

Note. — F_{24} and F_{70} are *Spitzer* MIPS 24 and *Herschel* PACS 70 μm fluxes except for the following sources: G74.0-8.5 (*IRAS* 25 and 60 μm fluxes); G189.1+3.0, G260.4-3.4, G315.4-2.3 (*Spitzer* MIPS 70 μm flux); G292.0+1.8, G304.6+0.1 (AKARI 65 μm flux). T_d is the color temperature for thermal dust emission, and F_{IR} is the integrated infrared flux. The numbers in parenthesis are 1σ errors.

Note. — F_{24} and F_{70} are *measured* (i.e., not color-corrected), background-subtracted fluxes of the *entire* SNR except the following sources:

G4.5+6.8: Flux of warm dust component in Tables 2 and 4 of Gomez et al. (2012).

G11.2-0.3: F_{70} is a bootstrapped flux from the 70 μm flux of the SNR shell (excluding the central area) using its F_{70}/F_{24} ratio.

G29.7-0.3: F_{70} is a bootstrapped flux from the 70 μm flux of the bright shell using its F_{70}/F_{24} ratio.

G41.1-0.3: F_{70} is a bootstrapped flux from the 70 μm flux of the bright eastern shell using its F_{70}/F_{24} ratio.

G111.7-2.1: F_{24} is from Hines et al. (2004) and F_{70} is the flux of the warm dust component in Table 1 of Barlow et al. (2010).

G120.1+1.4: Flux of warm dust component in Tables 3 and 4 of Gomez et al. (2012).

G304.6+0.1: Flux of the western shell in Table 4 of Lee et al. (2011). This is essentially equal to the total flux at wavelengths ≥ 60 μm .

G315.4-2.3: Flux of the NW region in Table 2 of Williams et al. (2011). This is a small fraction of the total flux.

G332.4-0.4: F_{70} is a bootstrapped flux from the 70 μm flux of the bright southern shell using its F_{70}/F_{24} ratio.

G349.7+0.2: Flux excluding the central bright source.

References. — References for 24 and 70 μm fluxes: (1) Gomez et al. (2012); (2) Braun & Strom (1986); (3) Hines et al. (2004); (4) Barlow et al. (2010); (5) Lee et al. (2009); (6) Lee et al. (2011); (7) Williams et al. (2011)

Table 2. X-ray Parameters of 20 SNRs.

SNR	Other Name	$N(\text{H})$ (10^{22} cm^{-2})	T_e (keV)	τ_{ion} ($10^{11} \text{ cm}^{-3} \text{ s}$)	F_X ($10^{-9} \text{ ergs cm}^{-2} \text{ s}^{-1}$)	Reference
G4.5+6.8	Kepler	0.52 (..., ...)	1.2 (..., ...)	1.1 (..., ...)	1.02 (..., ...)	2, 2, 2, 1
G11.2–0.3	...	2.2 (-0.4, 0.6)	0.7 (-0.1, 0.2)	0.86 (-0.19, 3.4)	0.87 (-0.42, 1.08)	1, 1, 1, 1
G15.9+0.2	...	3.9 (-0.2, 0.2)	0.9 (-0.1, 0.1)	0.54 (-0.14, 0.26)	0.46 (-0.01, 0.06)	3, 3, 3, 1
G27.4+0.0	Kes 73	2.35 (-0.15, 0.65)	0.75 (-0.15, 0.15)	0.90 (-0.1, 0.6)	0.43 (-0.07, 0.61)	1, 1, 1, 1
G29.7–0.3	Kes 75	3.96 (..., ...)	0.69 (-0.02, 0.01)	1.5 (-0.7, 0.7)	0.42 (..., ...)	4, 4, 4, 4
G31.9+0.0	3C391	3.1 (-0.1, 0.1)	0.56 (-0.01, 0.01)	≥ 12.8	0.49 (..., ...)	5, 5, 5, 5
G34.7–0.4	W44	1.0 (-0.2, 0.6)	0.88 (-0.14, 0.14)	2.0 (-0.7, 4.3)	0.64 (..., ...)	6, 6, 6, 6
G39.2–0.3	3C396	4.65 (-0.26, 0.11)	0.62 (-0.03, 0.1)	1.20 (-0.48, 0.66)	0.46 (..., ...)	7, 7, 7, 7
G41.1–0.3	3C397	3.05 (-0.2, 0.2)	0.21 (-0.01, 0.02)	1.4 (-0.6, 0.7)	27. (-6, 8)	8, 8, 8, 1
G43.3–0.2	W49B	5.2 (..., ...)	0.25 (-0.03, 0.03)	≥ 30	3.40 (..., ...)	9, 9, 9, 9
G74.0–8.5	Cygnus Loop	0.04 (..., ...)	0.23 (-0.01, 0.01)	2.0 (-0.1, 0.1)	9.98 (..., ...)	10,10,10,11
G111.7–2.1	Cas A	1.4 (-0.5, 0.5)	1.7 (-0.4, 0.4)	2.5 (-1.5, 1.5)	18.7 (..., ...)	12,13,13, 1
G120.1+1.4	Tycho	0.70 (..., ...)	0.85 (-0.15, 0.25)	1.00 (-0.21, 0.3)	6.7 (..., ...)	14,15,15, 1
G189.1+3.0	IC 443	0.69 (-0.15, 0.15)	0.42 (-0.16, 0.16)	≥ 10	2.9 (-1.3, 1.3)	16,16,16,16
G260.4–3.4	Puppis A	0.24 (-0.1, 0.11)	0.63 (-0.11, 0.1)	1.7 (-1, 1)	21. (..., ...)	17,17,17,18
G292.0+1.8	MSH 11–54	0.54 (-0.04, 0.04)	0.66 (-0.04, 0.12)	7.2 (-1.7, 2.5)	2.04 (-0.44, 0.58)	19,20,20, 1
G304.6+0.1	Kes 17	3.79 (-0.14, 0.03)	0.76 (-0.01, 0.03)	≥ 20	0.09 (..., ...)	21,21,21,21
G315.4–2.3	RCW 86	0.63 (-0.05, 0.03)	0.28 (-0.01, 0.02)	0.99 (-0.12, 0.12)	0.13 (..., ...)	22,22,22,22
G332.4–0.4	RCW 103	0.55 (-0.25, 0.15)	0.50 (-0.1, 0.1)	1.55 (-0.35, 0.95)	1.18 (-0.68, 0.13)	1, 1, 1, 1
G349.7+0.2	...	7.10 (-0.1, 0.1)	0.76 (-0.03, 0.05)	≥ 30	0.37 (..., ...)	23,23,23,23

Note. — $N(\text{H})$, T_e , τ_{ion} , and F_X are hydrogen absorbing columns, electron temperature, ionization timescale, and integrated (0.3–2.1 keV) X-ray flux, respectively. The numbers in parenthesis are 1σ errors. $N(\text{H})$ without errors indicates that it is fixed in the X-ray spectral analysis. For the other parameters, the numbers without errors indicate that the errors are not given in the references. When the CIE model is used for spectral analysis, we arbitrarily adopted $\tau_{\text{ion}} \geq 3 \times 10^{12} \text{ cm}^{-3} \text{ s}$.

Note. — All the parameters including F_X are for the *entire* SNRs except the following sources:
G29.7–0.3: T_e and τ_{ion} are average parameters of the diffuse and clump components in Table 4 of Helfand et al. (2003).
G41.1–0.3: T_e and τ_{ion} are average parameters of eastern and western lobes in Table 3 of Safi-Harb et al. (2005).
G43.3–0.2: T_e and τ_{ion} are those of the soft component in Table 2 of Kawasaki et al. (2005).
G189.1+3.0: Parameters are mean values of Shell A regions in Table 2 (see also Figure 7) of Troja et al. (2006). The flux is obtained by assuming a gas sphere of radius 7 pc with electron density $1.6 \pm 0.7 \text{ cm}^{-3}$ and a volume filling factor of 0.5 (cf. Troja et al. 2006).
G260.4–3.4: Flux from Dubner et al. (2013); other parameters are mean values of the regions (excluding ejecta knots) in Table 3 of Hwang et al. (2008).
G292.0+1.8: T_e and τ_{ion} are those of the circumstellar medium (region 1) in Table 1 of Park et al. (2004).
G315.4–2.3: Parameters of the NW shell in Table 1 of Williams et al. (2011).
G349.7+0.2: Parameters of the soft component in Table 2 of Lazendic et al. (2005).

References. — References for $N(\text{H})$, T_e , τ_{ion} , and F_X : (1) this work; (2) Burkey et al. (2013); (3) Reynolds et al. (2006); (4) Helfand et al. (2003); (5) Chen et al. (2004); (6) Harrus et al. (1997); (7) Harrus & Slane (1999); (8) Safi-Harb et al. (2005); (9) Kawasaki et al. (2005); (10) Tsunemi et al. (2007); (11) Ku et al. (1984); (12) Lee et al. (2014); (13) Hwang & Laming (2012); (14) Cassam-Chenaï et al. (2007); (15) Hwang & Gotthelf (1997); (16) Troja et al. (2006); (17) Hwang et al. (2008); (18) Dubner et al. (2013); (19) Lee et al. (2010); (20) Park et al. (2004); (21) Gelfand et al. (2013); (22) Williams et al. (2011); (23) Lazendic et al. (2005)

Table 3. Infrared-X-ray Correlation Parameters of 20 SNRs.

SNR	Other Name	SN type (MM?)	r_{50}	$R_{\text{IRX,obs}}$	$R_{\text{IRX,coll}}$
G4.5+6.8	Kepler	S	0.56	1.82 (-0.70, 1.05)	30.6 (..., ...)
G11.2–0.3	...	C	0.48	15.1 (-7.4, 18.8)	18.0 (-2.6, 6.2)
G15.9+0.2	...	S	0.42	9.59 (-0.56, 1.39)	20.2 (-2.4, 3.9)
G27.4+0.0	Kes 73	S?	0.45	20.8 (-3.6, 29.5)	19.2 (-3.5, 5.2)
G29.7–0.3	Kes 75	C	0.38	7.50 (-2.49, 2.76)	19.0 (-1.7, 0.6)
G31.9+0.0	3C391	S(y)	-0.49	58.8 (-17.8, 17.9)	≤ 8.78
G34.7–0.4	W44	C(y)	-0.55	203.8 (-62.8, 63.6)	24.3 (-6.8, 3.0)
G39.2–0.3	3C396	C(y)	-0.16	5.52 (-1.72, 1.76)	16.7 (-1.4, 3.3)
G41.1–0.3	3C397	S(y)	0.02	0.32 (-0.08, 0.10)	9.72 (-1.21, 2.55)
G43.3–0.2	W49B	S(y)	-0.59	15.0 (-4.6, 4.6)	≤ 2.41
G74.0–8.5	Cygnus Loop	S	0.40	12.3 (-3.9, 4.1)	8.63 (-0.27, 0.26)
G111.7–2.1	Cas A	S	0.30	1.74 (-0.59, 0.65)	50.2 (-18.4, 13.7)
G120.1+1.4	Tycho	S	0.20	0.75 (-0.29, 0.44)	21.5 (-3.6, 7.9)
G189.1+3.0	IC 443	C(y)	-0.15	27.8 (-12.8, 13.2)	≤ 7.87
G260.4–3.4	Puppis A	S	0.76	4.01 (-1.31, 1.42)	17.4 (-3.5, 3.0)
G292.0+1.8	MSH 11-54	S(y)	0.46	1.75 (-0.47, 0.67)	14.6 (-2.8, 4.6)
G304.6+0.1	Kes 17	S(y)	-0.28	43.4 (-14.5, 16.5)	≤ 9.15
G315.4–2.3	RCW 86	S	0.69	2.23 (-0.91, 1.68)	10.7 (-0.3, 0.3)
G332.4–0.4	RCW 103	S	0.47	15.8 (-9.4, 3.6)	13.8 (-2.6, 2.7)
G349.7+0.2	...	S(y)	0.05	81.6 (-25.3, 25.7)	≤ 6.58

Note. — The ‘(y)’ in SN type indicates that the SNR is of mixed-morphology, i.e., shell/composite-type in radio with center-filled thermal X-rays. See text for explanations of the other parameters.

Table 4. Shock Energy Conversion Efficiency of SNRs with Large IRX Flux Ratios

SNR	d (kpc)	R_s (pc)	L_X (L_\odot)	T_e (10^7 K)	$n_e\sqrt{f_V}$ (cm^{-3})	L_{IR} (L_\odot)	n_a (cm^{-3})	v_s (km s^{-1})	ϵ_{IR}
3C391	8.0	7.5	9.8e+02	0.65	2.04	7.5e+04	10	144	0.76
W44	3.0	11.0	1.8e+02	1.02	0.43	5.7e+04	3	152	0.64
W49B	11.4	6.6	1.4e+04	0.29	12.23	2.6e+05	10	237	0.80
IC 443	1.5	7.0	2.0e+02	0.49	1.14	1.5e+04	15	76	0.39
Kes17	10.0	10.0	2.8e+02	0.88	0.69	4.2e+04	10	98	0.24
G349.7+0.2	22.0	6.4	5.6e+03	0.88	6.04	4.4e+05	10	290	1.0

Note. — The conversion efficiency of shock energy to dust IR radiation ϵ_{IR} can be derived from the observed 0.3–2.1 keV X-ray (L_X) and IR (L_{IR}) luminosities, but depends on two uncertain parameters; the ambient density of H nuclei n_a and the volume filling factor of X-ray emitting gas f_V (see Equation 7). We fixed $f_V = 0.5$ and assumed $n_a = 10 \text{ cm}^{-3}$ except for the following sources:

W44: Park et al. (2013) obtained a mean density of 1.9 cm^{-3} and shocked speed of 135 km s^{-1} from HI observations. Chevalier (1999) reviewed available observations and concluded that $n_a = 4\text{--}5 \text{ cm}^{-3}$ and $v_s \sim 150 \text{ km s}^{-1}$. We adopt $n_a = 3 \text{ cm}^{-3}$.

IC 443: Chevalier (1999) reviewed available observations and concluded that $n_a \sim 15 \text{ cm}^{-3}$ and $v_s \sim 100 \text{ km s}^{-1}$. We adopt $n_a = 15 \text{ cm}^{-3}$.